Stability Characteristics of Deep-Water Replacement in the Strait of Georgia

RICHARD H. KARSTEN AND GORDON E. SWATERS

Applied Mathematics Institute, Department of Mathematical Sciences, University of Alberta, Edmonton, Alberta, Canada

RICHARD E. THOMSON

Institute of Ocean Sciences, Sidney, British Columbia, Canada

(Manuscript received 6 July 1994, in final form 21 March 1995)

ABSTRACT

It has been suggested that low-frequency current fluctuations in the southern Strait of Georgia are the result of baroclinic instability. However, data extracted from cyclesonde and fixed current meter moorings suggest that the conditions for baroclinic instability are highly variable in space and time. It has been recently discovered that there are summertime bottom-intensified gravity currents with fortnightly and monthly periods associated with the introduction of salty waters from the Juan de Fuca Strait during periods of neap tides. These currents are the dominant mechanism for deep-water renewal in the Strait of Georgia. It is argued that these currents are baroclinically unstable and that the stability characteristics are reasonably consistent with the observed structure of the low-frequency current fluctuations. The episodic nature of these unstable bottom flows may help to explain the spatial and temporal variability of the low-frequency current fluctuations observed in the Strait of Georgia.

1. Introduction

The origin and evolution of the low-frequency variability in the Strait of Georgia (SOG) are not completely understood (e.g., see the discussion in LeBlond 1983). In particular, many explanations have been proposed for the low-frequency current fluctuations that occur in the southern region of the SOG. The energy associated with these currents is known to be as important as that associated with the diurnal and semidiurnal tides (Chang et al. 1976). Helbig and Mysak (1976) initially suggested that the low-frequency variability could be described by bottom-trapped topographic planetary waves. However, a later analysis of available SOG data (Yao et al. 1982) showed that the vertical structure of the observed current fluctuations was inconsistent with the Helbig and Mysak model. Yao et al. (1982) also examined and dismissed the possibility that the low-frequency variability could be described by internal Kelvin waves.

Shortly afterward, Yao et al. (1985) proposed that the low-frequency current fluctuations were the result of a quasigeostrophic instability associated with the observed mean flow. However, the agreement between the theory and the observations was problematic since there were clearly times in the year when the observations did not satisfy various necessary conditions for quasigeostrophic instability (e.g., there were statistically insignificant correlations between the density and velocity fluctuations and there was no evidence of upward phase propagation of the disturbances), but the theory predicted instability nevertheless (Yao et al. 1985; Stacey et al. 1991).

In a series of subsequent papers, Stacey and colleagues (Stacey et al. 1987; Stacey et al. 1988; Stacey et al. 1991) presented and analyzed data taken from an array of cyclesonde and fixed current meters with sufficient spatial coverage to resolve the horizontal and vertical structure of the low-frequency variability in the southern part of the SOG. Their results were surprising in several respects. The fluctuations appear to have a relatively small horizontal length scale on the order of about 10 km (Stacey et al. 1987; see also Yao et al. 1985). Based on objectively produced streamfunction maps, Stacey et al. (1988) concluded that there was "unmistakable evidence" for the formation of subsurface eddies associated with the current fluctuations.

Stacey et al. (1991) addressed the issue of identifying an energy source for these low-frequency motions. Based on the Stacey et al. (1987) dataset, it was determined that the correlation between the density and current fluctuations was statistically significant, and of the correct sign for baroclinic instability, below approximately 160 m of depth. However, the appropriate correlations for instability were not observed at all moorings in the region examined. Stacey et al. (1991)

Corresponding author address: Dr. Gordon E. Swaters, Dept. of Math., Applied Math. Inst., University of Alberta, 632 Central Academic Building, Edmonton, Alberta T6G 2G1, Canada.
E-mail: gordon@hamal.math.ualberta.ca

concluded that if baroclinic instability is occurring, it is horizontally localized in space.

It would seem clear that if the observed subsurface eddies are the result of the baroclinic instability of a background current, it is an instability that occurs at depth but which is not uniformly distributed over the entire horizontal region or over the entire year. The problem then is to identify an unstable flow feature in the SOG that has these qualitative characteristics.

LeBlond et al. (1991) have established the existence in the SOG of summertime bottom-intensified currents that have fortnightly and monthly periods. These currents are the result of the introduction of salty waters from the Juan de Fuca Strait during periods of neap tides and are not formed during the winter months. They provide the dominant mechanism for deep-water renewal in the SOG. These currents flow northward on the eastern side of the SOG in the form of an elongated, bottom-trapped gravity current that is transversely confined in the across-strait direction. These currents therefore possess the property that they are not uniformly distributed in space and time. The principal purpose of this paper is to show that these gravity currents are unstable and that the stability characteristics of the most unstable modes are consistent with the observations.

Mesoscale gravity currents are formed when dense water is formed or otherwise released in a shallow sea, such as a shelf region, and settles to the bottom. If the bottom is sloping, then the combined influences of the Coriolis and buoyancy stresses may force the current to be transversely constrained and flow, in the Northern Hemisphere, with the direction of locally increasing bottom height to its right. Swaters (1991) developed a nonquasigeostrophic baroclinic instability theory for mesoscale gravity currents on a sloping bottom. The instability mechanism modeled by Swaters is the release of the available gravitational potential energy associated with a pool of relatively dense water sitting directly on a sloping bottom surrounded by relatively lighter water. As such, this instability mechanism is, phenomenologically, completely different than the shear-based instability associated with a buoyancy-driven current containing lighter water sitting on top of a finite lower layer (e.g., Paldor and Killworth 1987). The Swaters theory describes a purely baroclinic instability in that it filters out the shear-based instability and exclusively models the convective destabilization of a mesoscale gravity current on a sloping bottom.

Moreover, this instability model does not make the assumption, implicit in quasigeostrophic theory, that the dynamic deflections in the thickness of the gravity current are small in comparison to its scale height. By allowing for finite-amplitude deformations in the current height, the Swaters theory can describe the instability of gravity currents with isopycnals that intersect the bottom. In addition, the Swaters model does not require a zero in the transverse potential vorticity gradient for instability. The intrinsically baroclinic instability of the Swaters model differs from the nonbaroclinic instability identified by Griffiths et al. (1982) associated with a coupling of the two fronts in a mesoscale gravity current. [For a discussion comparing these two models, see Swaters (1991).] Numerical simulations based on the primitive equations (M. Kawase 1994, personal communication) suggest that the convective instability mechanism is two orders of magnitude more important than any other instability mechanism for mesoscale gravity currents.

Our results show that a model gravity current that reproduces the principal qualitative features of the deep-water replacement current in the SOG is baroclinically unstable. It turns out that the most important parameters in the stability calculation are the nondimensional width of the front relative to the internal deformation radius and a parameter, denoted μ, that measures the ratio of the maximum current height to the slope of the ambient topography. Physically, the parameter μ has a straightforward interpretation in that it measures, roughly speaking, the ratio of the destabilizing influence of baroclinic vortex-tube stretching in the nonfrontal layer to the stabilizing influence of the sloping bottom, which acts as a topographic β plane.

The plan of this paper is as follows. In section 2, we present the model and derive the linear stability equations and boundary conditions. In section 3, we briefly present some general stability properties of the linear stability and normal-mode equations. In section 4, we present our instability calculation for a model mesoscale gravity current on a wedge-shaped bottom. In section 5, we discuss how the solution depends on the various parameters and apply the model to the SOG. The paper is summarized in section 6.

2. Problem formulation

a. The governing equations

Since the derivation of the equations is very similar to that described by Swaters (1991), we will be brief in our presentation here. The basic model we assume is an f-plane, two-layer shallow-water system (both layers are assumed hydrostatic and homogeneous) with varying cross-channel topography (see Fig. 1).

If we denote the geostrophic pressure in the upper layer by $\eta(x, y, t)$, the height of the gravity current by $h(x, y, t)$, and the variable bottom topography by $h_B(y)$, the nondimensional governing equations can be written in the form

$$\Delta\eta_t + h_{B_y}(\eta_x + h_x) + \mu J(\eta, \Delta\eta) = 0, \quad (2.1)$$

$$h_t - h_{B_y} h_x + \mu J(\eta, h) = 0, \quad (2.2)$$

where $J(A, B) = A_x B_y - A_y B_x$, with x and y the alongchannel and cross-channel coordinates, respectively. The leading-order velocity fields in the upper and lower layers, denoted $\mathbf{u}_1(x, y, t)$ and $\mathbf{u}_2(x, y, t)$,

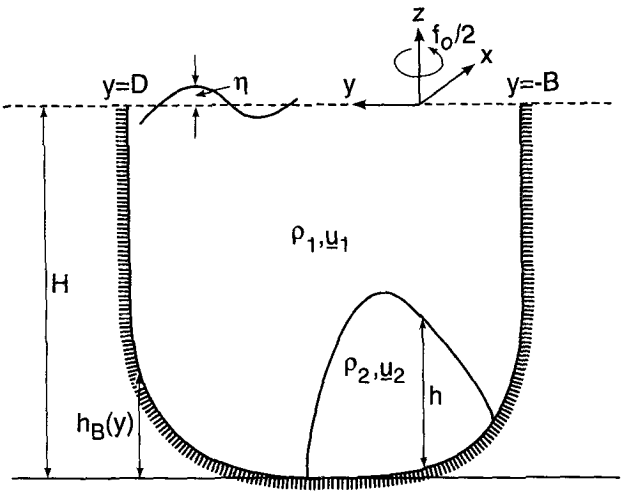

FIG. 1. The geometry of the two-layer system, in a channel with cross-channel topography given by $h_B(y)$ and walls at $y = -B, D$.

respectively, and the geostrophic pressure in the lower layer, denoted $p(x, y, t)$, are related to $\eta(x, y, t)$ and $h(x, y, t)$ via the relations

$$\mathbf{u}_1 = \hat{e}_3 \times \nabla\eta, \tag{2.3}$$

$$\mathbf{u}_2 = -h_{B_y}\hat{e}_1 + \mu\hat{e}_3 \times \nabla(\eta + h), \tag{2.4}$$

$$p = h_B + \mu(\eta + h), \tag{2.5}$$

where the parameter $\mu \equiv h_*/h_{B_*}$ with h_*, a scale height for the gravity current and h_{B_*}, a scale height for the variable bottom topography.

The parameter μ can be interpreted as measuring the ratio of the destabilizing influence of baroclinic vortex-tube stretching to the stabilizing influence of the variable bottom topography that acts as a background vorticity gradient (i.e., a topographic β plane). As it turns out, for a given along-channel mode, a minimum μ is required for instability.

If we denote the projection on the plane $z = 0$ of a particular intersection of the front height with the bottom by $\phi(x, y, t) = 0$, then the kinematic condition is given by

$$\phi_t - h_{B_y}\phi_x + \mu J(\eta + h, \phi) = 0, \tag{2.6}$$

on $\phi = 0$, and the frontal height must satisfy

$$h = 0 \tag{2.7}$$

on $\phi = 0$. Note that the determination of the evolution of $\phi(x, y, t)$ is part of the problem. The no-normal flow condition at the channel walls (see Fig. 1) is given by

$$\eta_x = 0 \quad \text{on} \quad y = -B, D. \tag{2.8}$$

Equation (2.1) [actually (2.1) + (2.2)] expresses the conservation of potential vorticity in the nonfrontal layer. Equation (2.2) expresses mass conservation for the gravity current with a geostrophically determined velocity field, which includes the effects of an upper layer and the gravitational acceleration associated with the sloping bottom. The derivation of these governing equations is identical to the formal asymptotic reduction of the two-layer, shallow-water equations presented in Swaters (1991), except that the bottom slope parameter s_* in Swaters (1991) would need to be replaced by h_{B_*}/L (where L is the horizontal length scale) to reflect the general topographic height retained here. This derivation is not included here and the reader is referred to Swaters (1991) for further details.

b. Linear stability equations and boundary conditions

It is straightforward to verify that (2.1)–(2.8) possess the exact steady alongchannel solution

$$h = \begin{cases} h_0(y), & a_1 < y < a_2 \\ 0, & -B < y < a_1 \quad \text{or} \quad a_2 < y < D, \end{cases}$$

$$\eta = \eta_0(y),$$

$$\phi = \begin{cases} \phi_1 = y - a_1 \\ \phi_2 = y - a_2. \end{cases} \tag{2.9}$$

In order to focus attention on the baroclinic instability of the gravity current and filter out any barotropic instability in the nonfrontal layer, we set $\eta_0 \equiv 0$.

The linear stability equations for this flow configuration are obtained by substituting

$$h = h_0(y) + h'(x, y, t),$$

$$\eta = \eta'(x, y, t),$$

$$\phi = \begin{cases} \phi_1 = y - a_1 - \phi_1'(x, t), \\ \phi_2 = y - a_2 - \phi_2'(x, t), \end{cases} \tag{2.10}$$

into the model equations and neglecting all quadratic and higher-order perturbation (primed) terms. In the region $a_1 < y < a_2$, the linearized equations take the form (henceforth, we shall drop the prime notation for the perturbation fields)

$$\Delta\eta_t + h_{B_y}(\eta_x + h_x) = 0, \tag{2.11}$$

$$h_t - h_{B_y}h_x + \mu h_{0_y}\eta_x = 0. \tag{2.12}$$

In the nonfrontal regions, $-B < y < a_1$ and $a_2 < y < D$, the stability problem for the channel water is simply

$$\Delta\eta_t + h_{B_y}\eta_x = 0. \tag{2.13}$$

The linearized and Taylor expanded boundary conditions are given by

$$h + h_{0_y}\phi_{1,2} = 0 \quad \text{on} \quad y = a_{1,2}, \tag{2.14}$$

$$\phi_{1,2_t} - (h_{B_y} + \mu h_{0_y})\phi_{1,2_x} - \mu(\eta + h)_x = 0 \quad \text{on} \quad y = a_{1,2}, \tag{2.15}$$

$$\eta_x = 0 \quad \text{on} \quad y = -B, D. \tag{2.16}$$

We also impose the condition that the channel-water perturbation pressure and normal mass flux be continuous at $y = a_1$ and $y = a_2$.

We have made the assumption that the current associated with the deep-water replacement in the SOG can be modeled with a function $h_0(y)$ that extends infinitely in the alongchannel direction. This is obviously an extremely crude model for a flow, which, in reality, is more like a pulse than a steady current. However, even though the water mass associated with the deep-water renewal extends finitely in both the alongchannel and cross-channel directions, the data clearly indicate that the cross-channel length scale is much smaller than the alongchannel length scale, so that this approximation is reasonable for the instability calculation presented here.

The data presented in Stacey et al. (1987) and further discussed by LeBlond et al. (1991) clearly indicate that the strong currents associated with the deep-water renewal are not uniformly distributed across the strait. If one uses the distance between the cyclesonde stations where the current was strongly observed and those where it was not so strongly observed, a crude estimate is that the cross-channel width of the current is no more than about 20 km.

On the other hand, the LeBlond et al. (1991) analysis of the data suggests that each pulse of deep-water renewal lasts continuously for about 10 days and propagates northward at a speed of about 18 cm s^{-1}. Geometrical considerations aside, this suggests that the alongchannel length scale of the pulse is about 150 km, which is roughly on the order of 10 times the current width.

c. *The normal-mode equations*

The normal-mode equations are obtained by assuming alongchannel propagating solutions of the form

$$[\eta, h, \phi_1, \phi] = [\tilde{\eta}(y), \tilde{h}(y), \tilde{\phi}_1, \tilde{\phi}_2] \times \exp[ik(x - ct)] + \text{c.c.}, \tag{2.17}$$

where c.c. means complex conjugate, k is the alongchannel wavenumber, and c is the alongfront complex phase speed. Substitution of (2.17) into (2.11) and (2.12) yields [after dropping the tildes and eliminating $\tilde{h}(y)$ in (2.18) using (2.19)]

$$c(\eta_{yy} - k^2\eta) - \left[h_{B_y} + \frac{\mu h_{B_y} h_{0_y}}{c + h_{B_y}}\right]\eta = 0, \tag{2.18}$$

$$h = \frac{\mu h_{0_y}}{c + h_{B_y}}\eta, \tag{2.19}$$

in the frontal region $a_1 < y < a_2$. We solve (2.18) for $\eta(y)$ and then compute $h(y)$ using (2.19) in this region.

In the nonfrontal regions where $-B < y < a_1$ and $a_2 < y < D$, the problem for $\eta(y)$ is given by

$$c(\eta_{yy} - k^2\eta) - h_{B_y}\eta = 0. \tag{2.20}$$

The boundary conditions at $y = a_{1,2}$ for the normal modes can be written in the form

$$h + h_{0_y}\phi_{1,2} = 0, \tag{2.21}$$

$$(c + h_{B_y})\phi_{1,2} = -\mu\eta, \tag{2.22}$$

where we have eliminated the $h(a_{1,2})$ term in (2.22) using (2.14). The boundary condition (2.16) becomes simply

$$\eta = 0 \quad \text{on} \quad y = -B, D. \tag{2.23}$$

In addition, we also require that the pressure and normal mass flux in the channel water be continuous across the frontal boundaries. Since there is no mean flow in the upper layer this is equivalent to requiring that η_y and η be continuous at $y = a_{1,2}$.

3. General stability characteristics

In this section, we derive some general stability results for the model equations. These results are useful in analyzing the detailed stability calculations presented in section 4. The reader who is not interested in these general derivations may go directly to section 4.

a. *Perturbation energetics*

If (2.11) and (2.13) are multiplied by $\eta(x, y, t)$ and subsequently integrated over $-B < y < D$ and $0 < x < \lambda$, where λ is the alongchannel wavelength of the perturbation, it follows (after integration by parts) that the averaged perturbation kinetic energy of the nonfrontal layer satisfies

$$\frac{\partial}{\partial t}\int_{-B}^{D}\langle\nabla\eta\cdot\nabla\eta\rangle dy = -2\int_{a_1}^{a_2} h_{B_y}\langle v_1 h\rangle dy, \tag{3.1}$$

where

$$\langle(*)\rangle = \lambda^{-1}\int_0^{\lambda}(*)dx.$$

It follows that if baroclinic instability occurs, then on average the correlation between the perturbation cross-channel velocity in the channel water, the frontal height anomaly, and the channel-bottom slope must be negative. If we assume that on average the channel bottom slopes downward toward the center of the channel, then, as found in Swaters (1991), a necessary condition for instability is a net transport of heat toward the channel walls. Since the bottom slope is equivalent to a topographic β plane, we can interpret a net flux of heat toward the walls, that is, up the sloped bottom, as equivalent to the northward flux of heat required in midlatitude baroclinic instability (LeBlond and Mysak, section 44).

If (2.12) is multiplied by $h_{B_y}h$, then we can form the balance

$$\frac{\partial}{\partial t}\int_{a_1}^{a_2}\frac{h_{B_y}^2}{\mu h_{B_y}h_{0_y}}\langle h^2\rangle dy = -2\int_{a_1}^{a_2} h_{B_y}\langle v_1 h\rangle dy. \quad (3.2)$$

This expression and (3.1) can be combined to form

$$\frac{\partial}{\partial t}\left[\int_{-B}^{D}\langle\nabla\eta\cdot\nabla\eta\rangle dy - \int_{a_1}^{a_2}\frac{h_{B_y}^2}{\mu h_{B_y}h_{0_y}}\langle h^2\rangle dy\right] = 0. \quad (3.3)$$

It immediately follows that instability can only occur if $h_{B_y}(y)h_{0_y}(y) > 0$ for some value of $y \in (a_1, a_2)$. Conversely, it follows that if $h_{B_y}(y)h_{0_y}(y) \leq 0$ for all $y \in (a_1, a_2)$, then the front is linearly stable.

b. General stability results for the normal modes

By multiplying (2.18) and (2.20) by the complex conjugate of $\eta(y)$, integrating the result over $-B < y < D$, and adding the two equations together, it is possible to form the balance (after integration by parts):

$$\int_{-B}^{D}\left\{c|\eta_y|^2 + \left[ck^2 + h_{B_y} + \Theta(y)\mu h_{B_y}h_{0_y} \times \frac{(c^* + h_{B_y})}{|c + h_{B_y}|^2}\right]|\eta|^2\right\}dy = 0, \quad (3.4)$$

where $\Theta(y) = 1$ for $a_1 < y < a_2$ and $\Theta(y) = 0$ for $-B < y \leq a_1$ and $a_2 \leq y < D$, and c^* is the complex conjugate of $c = c_R + ic_I$. The imaginary and real parts of (3.4) are given by, respectively,

$$c_I\left\{\int_{-B}^{D}\left[|\eta_y|^2 + \left(k^2 - \frac{\Theta(y)\mu h_{B_y}h_{0_y}}{|c + h_{B_y}|^2}\right)|\eta|^2\right]dy\right\} = 0, \quad (3.5)$$

$$c_R\left\{\int_{-B}^{D}\left[|\eta_y|^2 + \left(k^2 + \frac{\Theta(y)\mu h_{B_y}h_{0_y}}{|c + h_{B_y}|^2}\right)|\eta|^2\right]dy\right\} = -\int_{-B}^{D}\left[1 + \frac{\Theta(y)\mu h_{B_y}h_{0_y}}{|c + h_{B_y}|^2}\right]h_{B_y}|\eta|^2 dy. \quad (3.6)$$

We see again that from (3.5) a necessary condition for instability is that $h_{B_y}(y)h_{0_y}(y) > 0$ for some value of $a_1 < y < a_2$. Consequently, assuming that instability occurs, we may set

$$\max_{y\in(a_1,a_2)}[h_{B_y}(y)h_{0_y}(y)] = \gamma^2 > 0, \quad (3.7)$$

where $\gamma > 0$, which will be used momentarily.

Assuming that instability occurs, the expression inside the curly brackets in (3.5) must be identically zero and can be rearranged into the form

$$\int_{a_1}^{a_2}\frac{h_{B_y}h_{0_y}}{|c + h_{B_y}|^2}|\eta|^2 dy = \frac{Q}{\mu}, \quad (3.8)$$

where

$$Q \equiv \int_{-B}^{D}(|\eta_y|^2 + k^2|\eta|^2)dy, \quad (3.9)$$

which is just the kinetic energy of the perturbation field in the channel water. However, using (3.7) it follows from (3.8) that

$$\int_{a_1}^{a_2}\frac{|\eta|^2}{|c + h_{B_y}|^2}dy \geq \frac{Q}{\mu\gamma^2},$$

which can be rearranged to imply

$$\begin{aligned}\min_{y\in(a_1,a_2)}|c + h_{B_y}|^2 &\leq \mu\gamma^2 Q^{-1}\int_{a_1}^{a_2}|\eta|^2 dy,\\ &\leq \mu\gamma^2 Q^{-1}\int_{-B}^{D}|\eta|^2 dy,\\ &= \left(\frac{\mu\gamma^2}{k^2}\right)Q^{-1}\int_{-B}^{D}k^2|\eta|^2 dy,\\ &\leq \frac{\mu\gamma^2}{k^2}.\end{aligned} \quad (3.10)$$

If we now assume that

$$\max_{y\in(a_1,a_2)}h_{B_y}(y) = \alpha_1 \quad \text{and} \quad \min_{y\in(a_1,a_2)}h_{B_y}(y) = \alpha_2, \quad (3.11)$$

where $-\infty < \alpha_2 \leq \alpha_1 < \infty$, it follows from (3.10) that if instability occurs, then the complex phase speed must lie in the region defined by

$$\begin{cases}(c_R + \alpha_1)^2 + c_I^2 \leq \dfrac{\mu\gamma^2}{k^2}, & \text{if} \quad c_R < -\alpha_1,\\ c_I^2 \leq \dfrac{\mu\gamma^2}{k^2}, & \text{if} \quad -\alpha_1 \leq c_R \leq -\alpha_2,\\ (c_R + \alpha_2)^2 + c_I^2 \leq \dfrac{\mu\gamma^2}{k^2}, & \text{if} \quad c_R > -\alpha_2,\end{cases} \quad (3.12)$$

where $c_I \geq 0$ and γ^2 is determined from (3.7). The region represents a rectangle of length $\alpha_1 - \alpha_2$ with a quarter circle on each end, with the height of the rectangle and the radius of the circles given by $\mu^{1/2}\gamma/k$. Note that the area of the region will increase with increasing μ, but will decrease with increasing alongfront wavenumber k. Also, it follows from (3.12) that the growth rate satisfies

$$\sigma = kc_I \leq \gamma\mu^{1/2}. \quad (3.13)$$

We can get alternative bounds on the real part of the phase speed as follows. Assuming instability occurs,

we may use (3.8) to simplify (3.6). The result can be written in the form

$$c_R = -(2Q)^{-1}\left\{\int_{-B}^{D}\left[1+\frac{\Theta(y)\mu h_{B_y}h_{0_y}}{|c+h_{B_y}|^2}\right]h_{B_y}|\eta|^2dy\right\}. \tag{3.14}$$

From (3.14) a second set of bounds on the real phase speed can be determined. These bounds together with (3.12) can be used to infer the existence of a high wavenumber cutoff. The details are similar to those presented in Swaters (1991) and are omitted. In the next section, we will explicitly compute the high wavenumber cutoff for a wedge-shaped bottom profile.

4. Stability calculation for a parabolic gravity current on a wedge-shaped bottom

The available data is unfortunately not able to resolve the detailed cross-channel shape of the gravity current associated with the deep-water replacement in SOG. Nevertheless, much can be learned from determining the stability characteristics associated with a model gravity current given by

$$h_0(y) = 1 - 4\left(\frac{y-a}{l}\right)^2, \tag{4.1}$$

where $l \equiv a_2 - a_1$ is the width and $a \equiv (a_1 + a_2)/2$ is the midpoint of the unperturbed current. Note that $h_0(a) = 1$, which means that the scale current height is chosen as the maximum dimensional height of the unperturbed current. The model (4.1) allows for the gravity current height to intersect the bottom in a coupled-front configuration. In section 5, we will choose values of a and l so that our model will closely approximate the current described in the volume flux estimates of LeBlond et al. (1991).

The bottom bathymetry in the region of the SOG where the Stacey et al. (1987) dataset was collected can be reasonably well modeled with a wedge-shaped bottom of the form

$$h_B(y) = \begin{cases} -s_1 y, & -B < y < 0 \\ s_2 y, & 0 < y < D. \end{cases} \tag{4.2}$$

We consider only the case where the gravity current lies entirely on one side of the channel, that is, when it lies entirely in either the $y < 0$ or $y > 0$ region. The case where the current spans $y = 0$ will not be discussed because the linearization of the problem fails across the discontinuity in h_{B_y} at $y = 0$. Since the problem is symmetric in y we will study only the case where $a_2 < 0$. This implies that we may choose $h_{B_*} = s_1^* L$, so that $s_1 = (L/h_{B_*})s_1^* = 1$. Values for the parameters s_2, B, and D will be discussed in section 5.

a. Derivation of the dispersion relation

Substitution of $h_B(y)$ given by (4.2) and $h_0(y)$ given by (4.1) into the normal-mode equations (2.18) and (2.20) yields the equations

$$\eta_{yy} - \left\{k^2 - \frac{1}{c}\right\}\eta = 0, \quad \text{for} \quad -B < y < a_1 \tag{4.3}$$

$$\eta_{yy} - \left\{k^2 - \frac{1}{c} + \frac{8\mu(y-a)}{c(c-1)l^2}\right\}\eta = 0, \quad \text{for} \quad a_1 < y < a_2 \tag{4.4}$$

$$\eta_{yy} - \left\{k^2 - \frac{1}{c}\right\}\eta = 0, \quad \text{for} \quad a_2 < y < 0 \tag{4.5}$$

$$\eta_{yy} - \left\{k^2 + \frac{s_2}{c}\right\}\eta = 0, \quad \text{for} \quad 0 < y < D, \tag{4.6}$$

with the boundary conditions

$$\eta = 0 \quad \text{on} \quad y = -B, D, \tag{4.7}$$

and the pressure and mass flux matching conditions

$$[\eta] = [\eta_y] = 0 \quad \text{on} \quad y = a_{1,2}. \tag{4.8}$$

The general solution to (4.4) may be written in the form

$$\eta(y) = C_1 A_i[\xi(y)] + C_2 B_i[\xi(y)], \quad \text{for} \quad a_1 < y < a_2, \tag{4.9}$$

where $A_i(\xi)$ and $B_i(\xi)$ are Airy functions (Abramowitz and Stegun 1972, section 10.4) with argument $\xi(y)$ given by

$$\xi(y) = \left[\frac{c(c-1)l^2}{8\mu}\right]^{2/3}\left[k^2 - \frac{1}{c} + \frac{8\mu(y-a)}{c(c-1)l^2}\right], \tag{4.10}$$

and where C_1 and C_2 are, as yet, undetermined coefficients. Using (4.7), the solutions to (4.3), (4.5), and (4.6) respectively, may be written in the form

$$\eta(y) = C_3 \sinh\left[\left(k^2 - \frac{1}{c}\right)^{1/2}(y+B)\right], \quad \text{for} \quad -B < y < a_1, \tag{4.11}$$

$$\eta(y) = C_4 \exp\left[-\left(k^2 - \frac{1}{c}\right)^{1/2} y\right] + C_5 \times \exp\left[\left(k^2 - \frac{1}{c}\right)^{1/2} y\right], \quad \text{for} \quad a_2 < y < 0, \tag{4.12}$$

$$\eta(y) = C_6 \sinh\left[\left(k^2 + \frac{s_2}{c}\right)^{1/2}(y-D)\right], \quad \text{for} \quad 0 < y < D, \tag{4.13}$$

where C_3, C_4, C_5, and C_6 are additional, as yet, undetermined coefficients. We take our branch cut in the complex plane along the negative real axis.

The application of the matching conditions (4.8) is straightforward and leads to a system of six homogeneous equations in the unknown coefficients C_1, C_2, C_3, C_4, C_5, and C_6. This system can be most conveniently written in the matrix form

$$\mathbf{M}\cdot\mathbf{C} = 0, \tag{4.14}$$

where $\mathbf{C} = (C_1, C_2, C_3, C_4, C_5, C_6)^{\mathrm{T}}$ (a column vector) and $\mathbf{M}$ is a 6×6 matrix determined by (4.9), (4.11), (4.12), and (4.13).

For a nontrivial solution of (4.14), we require

$$\det(\mathbf{M}) = 0, \tag{4.15}$$

which forms the complex dispersion relationship for the normal-mode solutions. We may consider that (4.15) implicitly defines a seven-parameter dispersion relationship of the form

$$c = c(k, \mu, a, l, s_2, B, D). \tag{4.16}$$

(In the above formulas, we can use $a_1 = a - l/2$ and $a_2 = a + l/2$ since the front is symmetric about a.)

Assuming that (4.15) is solved, we may determine the coefficients C_2, C_3, C_4, C_5, and C_6 as functions of the single free coefficient C_1. With $\eta(y)$ determined as described here, the perturbation frontal thickness $h(y)$ will be given by [see (2.19)]

$$h(y) = -\frac{8\mu(y-a)\eta(y)}{l^2(c-1)}, \tag{4.17}$$

in the region $a_1 < y < a_2$, and the amplitude of the perturbation frontal boundaries will be given by [see (2.22)]

$$\phi_{1,2} = -\frac{\mu\eta(a_{1,2})}{c-1}, \tag{4.18}$$

at $y = a_1$ and a_2, respectively. Finally, with the complex normal-mode amplitudes determined, the *real* valued solutions are obtained by substituting these amplitude functions into (2.17).

b. *High wavenumber cutoff and minimum interaction parameter estimates*

For this model, it is possible to explicitly determine a semicircle of instability, a high wavenumber cutoff, and a minimum μ needed for instability based on the theory developed in section 3b. For the parabolic front (4.1), it follows using (3.7) that the region of instability described by (3.12) reduces to the semicircle region given by

$$(c_R - 1)^2 + c_I^2 \leq \frac{4\mu}{lk^2}, \tag{4.19}$$

which gives the growth rate bound

$$\sigma \leq \frac{2\mu^{1/2}}{l^{1/2}}. \tag{4.20}$$

It follows from (3.14) that the real part of the phase speed will satisfy

$$c_R = \frac{1}{2} + (2Q)^{-1} \times \left\{ \int_{-B}^{0} |\eta|^2 dy - s_2 \int_{0}^{D} |\eta|^2 dy \right\}, \tag{4.21}$$

which implies that

$$\frac{1}{2} - \frac{s_2}{2k^2} \leq c_R \leq \frac{1}{2} + \frac{1}{2k^2}. \tag{4.22}$$

However, it also follows from (4.19) that the real part of the complex phase speed of an unstable mode must lie in the interval

$$1 - \frac{2\mu^{1/2}}{kl^{1/2}} \leq c_R \leq 1 + \frac{2\mu^{1/2}}{kl^{1/2}}. \tag{4.23}$$

Clearly, for sufficiently large alongfront wavenumbers (for given μ, l) the intervals (4.22) and (4.23) will be disjoint since the interval in (4.22) collapses to a small neighborhood centered at $c_R = 1/2$ and (4.23) collapses to a small neighborhood centered at $c_R = 1$. Consequently, it follows that instability can only occur when

$$\frac{1}{2}\left(1 + \frac{1}{k^2}\right) \geq 1 - \frac{2\mu^{1/2}}{kl^{1/2}}, \tag{4.24}$$

which is the necessary and sufficient condition for the intersection of the two intervals (4.22) and (4.23) to be nonempty. The inequality (4.24) can be rearranged to imply that the wavenumber of an unstable mode must satisfy

$$k \leq k_{\max} = \frac{2\mu^{1/2} + (l + 4\mu)^{1/2}}{l^{1/2}}. \tag{4.25}$$

The value of $k_{\max}$ given by (4.25) is an overestimate of the actual high wavenumber cutoff.

Given a particular wavenumber, the estimated minimum μ needed for instability as determined by (4.24) is given by

$$\mu_{\min} = \frac{l(k^2-1)^2}{16k^2}, \tag{4.26}$$

if $k > 1$ and $\mu_{\min} = 0$ for $0 \leq k \leq 1$. The value of $\mu_{\min}$ in (4.26) is an underestimate.

5. Description of the solutions and application to the Strait of Georgia

a. General discussion

In this section, we choose "typical" values for the parameters in (4.16). Using these values, we present the solution to the dispersion relation and discuss the stability characteristics. We also examine the effect of changing the parameters. As it turns out, the single most important parameter that influences the stability characteristics is the baroclinic stretching parameter μ.

We will choose the typical parameter values to reflect the physical characteristics of the strait and the current at the cyclesonde station where the current was most strongly observed [see station number 3 in LeBlond et al. (1991)]. The nondimensionalization scheme used to derive (see Swaters 1991 for details) the governing model equations (2.1) and (2.2) uses the internal deformation radius based on the total mean depth of the nonfrontal layer and the Nof speed (Nof 1983) as the horizontal length and velocity scales, respectively. Taking the averaged observed velocity as the Nof speed gives the velocity scale of $U \approx 18$ cm s^{-1}. Using a representative depth of the strait, $H \approx 300$ m, and an average bottom slope $s_1^* \approx 9$ m km^{-1} at the observation point, we obtain an estimate of the horizontal length scale, $L = (HU/f_0 s_1^*)^{1/2} \approx 7$ km. Time is scaled advectively giving a timescale of approximately $T \approx 11$ hours. We will denote dimensional quantities with an asterisk; for example, the nondimensional phase velocity is denoted c and the dimensional analogue is c^*, and so on.

We will model the strait as a channel of width 28 km with its center 21 km from the eastern wall. The bottom slope on the eastern and western side of the strait are taken to be 9 and 18 m km^{-1}, respectively. Based on estimates in LeBlond et al. (1991), we choose the maximum current height to be 65 m and the current width to be 14 km. We will assume that the current lies completely on the eastern side of the channel with its center located at the station 3 cyclesonde (see Stacey et al. 1987 or LeBlond et al. 1991), which is about 8.75 km from the center of the channel. In Fig. 2, we show the geometry used to model the gravity current in the SOG.

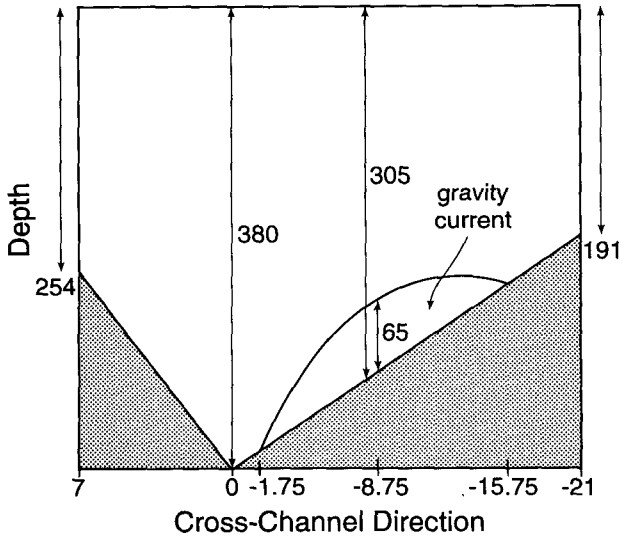

FIG. 2. Geometry of the gravity current model used for the Strait of Georgia in dimensional units. The horizontal lengths are in kilometers and the depths in meters.

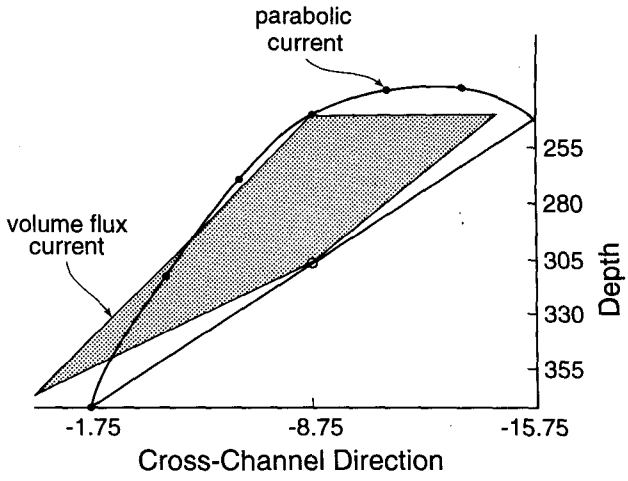

FIG. 3. A comparison of the parabolic gravity current model used in this paper with the volume-flux current used in LeBlond et al. (1991). The horizontal lengths are in kilometers and the depths in meters.

LeBlond et al. (1991), in estimating the volume flux of the gravity current, used a model current with a trapezoidal cross section. In Fig. 3, we compare our parabolic current profile to their trapezoidal current profile. Using this model, we estimate that typical nondimensional parameter values would be given by

$$\mu = 1.0, \quad a = -1.25, \quad s_2 = 2.0,$$

$$l = 2.0, \quad B = 3.0, \quad D = 1.0.$$

In Fig. 4, we present the nondimensional growth rate, frequency, and phase speed obtained from the dispersion relationship versus the wavenumber for the typical parameter values as given above. The graph is plotted over the interval $0 \leq k \leq k_{\max}$, where $k_{\max}$ is given by (4.25). Note that the actual high wavenumber cutoff is less than that given by (4.25). The most unstable mode occurs at $k \approx 1.1$, with the corresponding growth rate $\sigma \approx 0.46$, phase velocity $c_R \approx 0.65$, and frequency $\omega \approx 0.72$. In dimensional terms, this corresponds to a wavelength of approximately 40 km, an e-folding timescale of approximately 1 day, a phase speed of approximately 12 cm s^{-1}, and a period of approximately 4 days. The stability boundary (i.e., the actual high wavenumber cutoff) corresponds to a wavelength of about

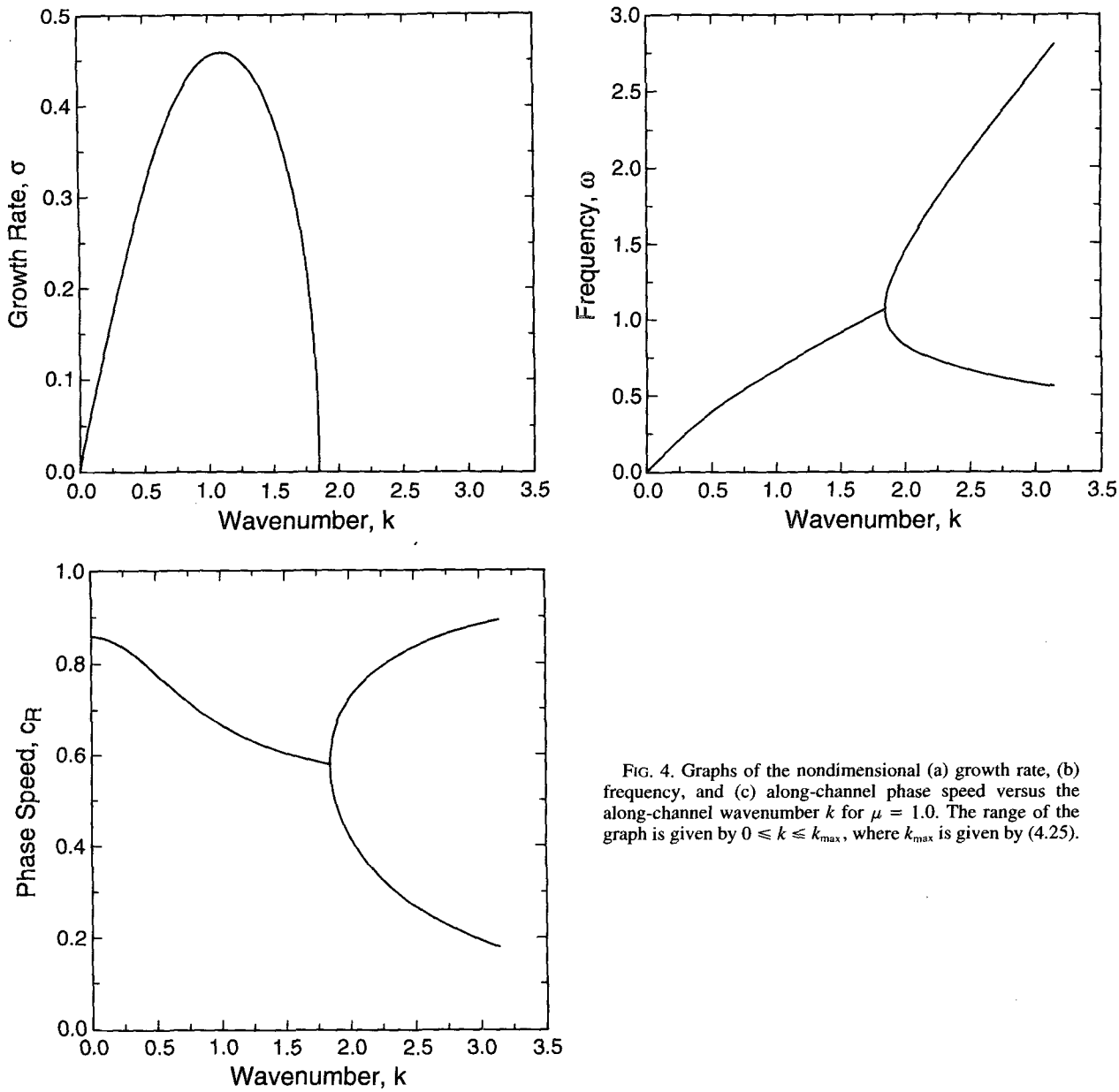

FIG. 4. Graphs of the nondimensional (a) growth rate, (b) frequency, and (c) along-channel phase speed versus the along-channel wavenumber k for $\mu = 1.0$. The range of the graph is given by $0 \leq k \leq k_{max}$, where k_{max} is given by (4.25).

24 km. Thus, all modes with wavelength longer than about 24 km are unstable.

This is a relatively rapidly growing instability. As this mode grows, nonlinear effects eventually come to dominate the evolution. These nonlinear effects could lead to further destabilization and even smaller length-scale eddylike features could develop or they could stabilize the instability. Assuming that the stabilized eddylike anomalies would have length scales of about a half-wavelength, our calculations suggest the finite-amplitude anomalies would have a length scale of about 20 km. This value is somewhat larger than the objective analysis of Stacey et al. (1988) would suggest, but is reasonably consistent nonetheless given our uncertainty in the parameter estimates and the sensitivity of the calculation to the parameter values.

Next we examine how the stability characteristics change as the parameters are varied. We will concentrate on how parameter variations lead to changes in the high wavenumber cutoff and the wavenumber and growth rate of the most unstable mode.

The parameter μ has the most direct impact on the stability characteristics. This parameter reflects changes in the scale frontal height and bottom topography and therefore, reflects changes in two of the more variable aspects of the flow geometry that we had to estimate. In Fig. 5a, we plot the calculated maximum growth rate wavenumber, the high wavenumber cutoff

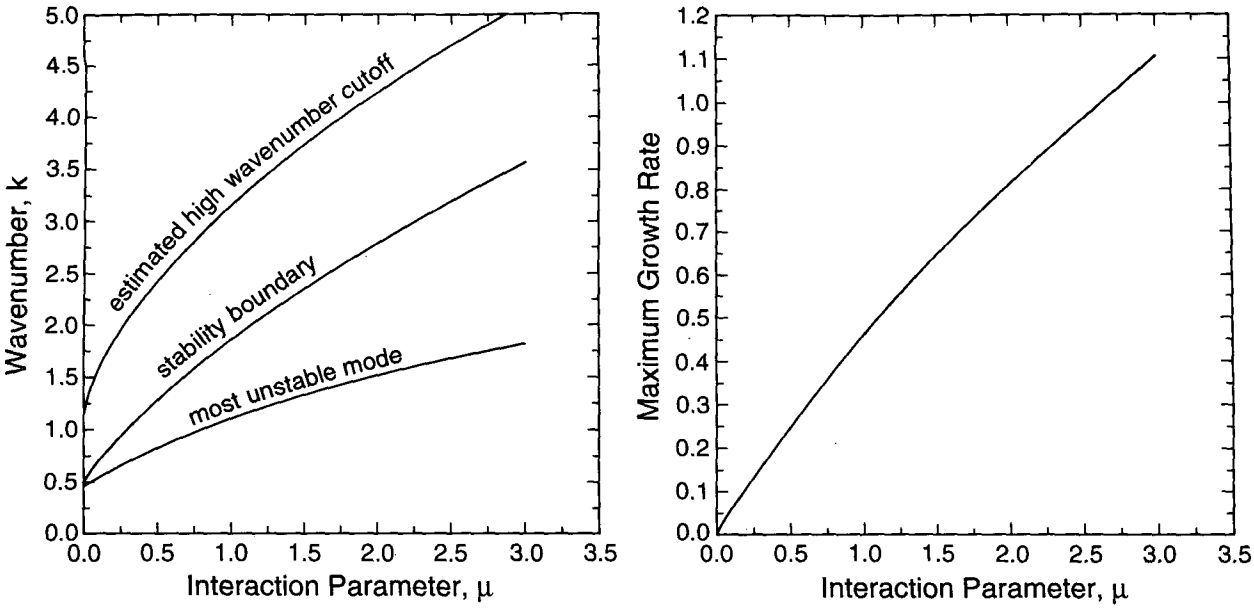

FIG. 5. (a) (from bottom to top) The wavenumber of the most unstable mode, the actual stability boundary, and the predicted high wavenumber cutoff as given by (4.25) versus the parameter μ. (b) The maximum growth rate versus μ.

(i.e., the actual stability boundary) and the predicted high wavenumber cutoff as given by (4.25) versus the parameter μ.

For a given value of μ, all wavenumbers less than the wavenumber of the stability boundary correspond to unstable modes. Hence, as μ increases there is an increasing band of wavenumbers that are unstable. In addition, as μ increases we see that the wavenumber of the most unstable mode also increases, which implies that the length scale of the instabilities would decrease with increasing μ. The parameter μ can be directly related to the slope of the bottom since

$$\mu = \frac{h_*}{h_{B_*}} = \frac{h_*}{s_1^* L},$$

[see the discussion after (4.2)]. Thus, reducing the slope s_1^* increases μ, and we conclude that decreasing the local bottom slope decreases the wavelength of the most unstable mode. This is of interest because the current array deployed by Stacey et al. (1987) is located in a region where the local bottom slope is decreasing in the northward direction. We suggest that the small-scale subsurface eddy features observed in the objective analysis of Stacey et al. (1988) may correspond to instabilities of the sort described here, which rapidly develop into smaller-scale structures due to the locally decreasing bottom slope as the destabilized pulses of deep water move northward on the eastern side of the strait.

Note also that Fig. 5a clearly shows that the actual high wavenumber cutoff is less than the predicted one as expected, but it also shows that (4.25) gives a relatively accurate prediction of $k_{\max}$. The high wavenumber cutoff and most unstable mode wavenumber grow like $\mu^{1/2}$ as (4.25) suggests.

In Fig. 5b, we plot the maximum growth rate versus the parameter μ. Clearly, increasing the value of μ increases the growth rate of the most unstable mode. The maximum growth rate appears to grow linearly in μ for these small values of μ rather than like $\mu^{1/2}$, as suggested by (4.20). This implies that a higher front or a flatter bottom would result in a more rapidly developing instability at a shorter wavelength. For example at $\mu = 2.0$ or 3.0, values that could reasonably occur in the flat central section of the SOG (see LeBlond et al. 1991), the wavelength of the most unstable mode becomes approximately 29 and 24 km, respectively, and the e-folding time is about 14 and 10 hours, respectively. Thus, it is plausible that once the deep-water replacement current goes unstable and the anomalies propagate northward, the along-channel variations in the bottom slope may act to increase growth rates and shorten the length scales of the perturbations leading to smaller length scale current fluctuations. This is a scenario that is completely consistent with the suggestion of Stacey et al. (1991) that the low-frequency current fluctuations look more like geostrophic turbulence than wavelike features. It should be noted that as μ becomes very large, $\mu \geq 8$, a second mode of instability develops with an even more complicated horizontal structure. This second mode is not likely to occur in the SOG, and the reader is referred to Swaters (1991) for further details.

Changing the width of the front also has a noticeable effect on the stability characteristics. In Fig. 6, we examine the effect of the frontal width on the growth rate of the most unstable mode. We see that as l increases

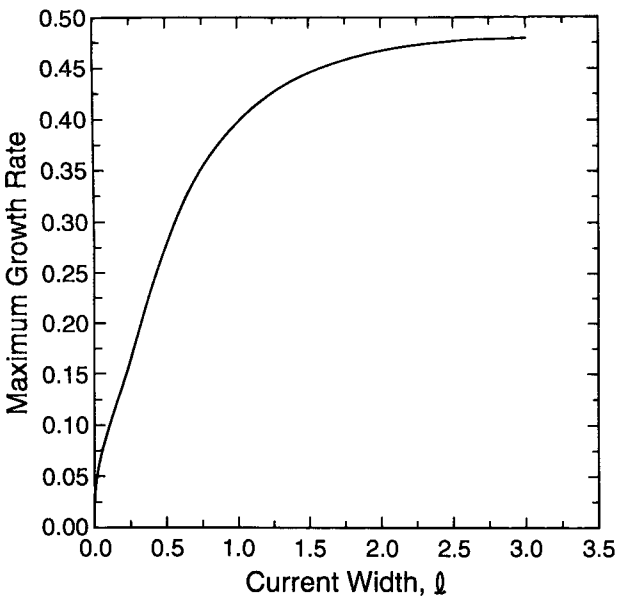

FIG. 6. Graph of the maximum growth rate versus the current width parameter l.

the growth rate of the most unstable mode also increases. We conclude that broader gravity currents experience a more rapid destabilization than narrower currents for the same maximum current height.

Note that at first appearance, (4.20) and Fig. 6 contradict each other. From Fig. 6, we see that the growth rate decreases as l decreases, but (4.20) suggests the upper bound increases. The figure shows the correct behavior since if no front exists; that is, $l = 0$, then there is no source of instability in the model. The problem with (4.20) is that it has been derived assuming $c_l \neq 0$. In fact, it follows from (3.5) that in the limit $l \to 0$; that is, $a_1 \to a_2$, that $c_l \to 0$ since

$$\lim_{a_2 \to a_1} \int_{a_1}^{a_2} \frac{h_{B_y} h_{0_y}}{|c + h_{B_y}|^2} |\eta|^2 dy$$

$$= \lim_{a_2 \to a_1} \frac{1}{|c+1|^2} \int_{a_1}^{a_2} \frac{-8y + 4(a_1 + a_2)}{(a_2 - a_1)^2} |\eta|^2 dy$$

$$= \lim_{a_2 \to a_1} \frac{1}{|c+1|^2} \frac{\int_{a_1}^{a_2} [-8y + 4(a_1 + a_2)] |\eta|^2 dy}{(a_2 - a_1)^2}$$

$$= \frac{1}{|c+1|^2} \times \lim_{a_2 \to a_1} \frac{-4(a_2 - a_1)|\eta(a_2)|^2 + 4\int_{a_1}^{a_2} |\eta|^2 dy}{2(a_2 - a_1)}$$

$$= \frac{1}{|c+1|^2} (-2|\eta(a_1)|^2 + 2|\eta(a_1)|^2) = 0.$$

This fact together with (3.5) implies that $c_l Q = 0$, where Q is given by (3.9), which in turn implies $c_l \equiv 0$ for a nontrivial mode.

Changing the placement of the channel walls at $y = -B$ and $y = D$, the placement of the center of the front at $y = a$, and the western bottom slope, s_2, has little effect on the solutions. Only when $D \to 0$, or $s_2 \to \infty$, and the down slope edge of the front nears the center of the channel, is there a noticeable effect. In these situations the western wall, or steeply sloped bottom, prevents the slumping action of the current, and thus inhibits instability. These are extreme situations and not of relevance to the SOG. Thus, we see that it is the parameter μ and, to a lesser extent, the frontal width l that are most important in determining the characteristics of the solution.

b. Spatial structure of the unstable modes

In this section we describe the spatial structure of the most unstable mode for the typical parameter values. To effectively illustrate what the shape of an unstable gravity current is according to our theory, we will introduce a sufficiently large perturbation amplitude. In what follows we have chosen the free coefficient C_1 in (4.9) so that the maximum perturbation height is approximately one.

In Fig. 7a, we depict the perturbation pressure field in the upper layer. The anomalies take the form of alternating cyclones and anticyclones. The wave field can be thought of as essentially an amplifying topographic planetary wave. The local extrema in the pressure field are centered near the downslope edge of the unperturbed front located at $y = a_2 = -0.25$. This reflects the fact that the amplitude of the instability is maximized at precisely the location where there is the maximum release of local available potential energy. The wave field propagates in the positive x direction.

In Fig. 7b, we depict the *total* height of the perturbed gravity current. The most important feature to note here is that the current boundary on the offshore or downslope side is substantially deformed in comparison to the onshore or upslope side. This reflects, again, the fact that the energetics of the instability is the release of the available potential energy associated with the downslope "slumping" of the gravity current. Note also, that if we compare Fig. 7a with Fig. 7b, the local extrema in the upper layer are displaced slightly in the positive x direction. This, of course, reflects nothing more than a "westward" phase shift with height associated with an unstable baroclinic wave (recall the sloping bottom acts like a topographic β plane).

6. Summary and conclusions

We have presented a theoretical calculation for the baroclinic instability of the mesoscale gravity current

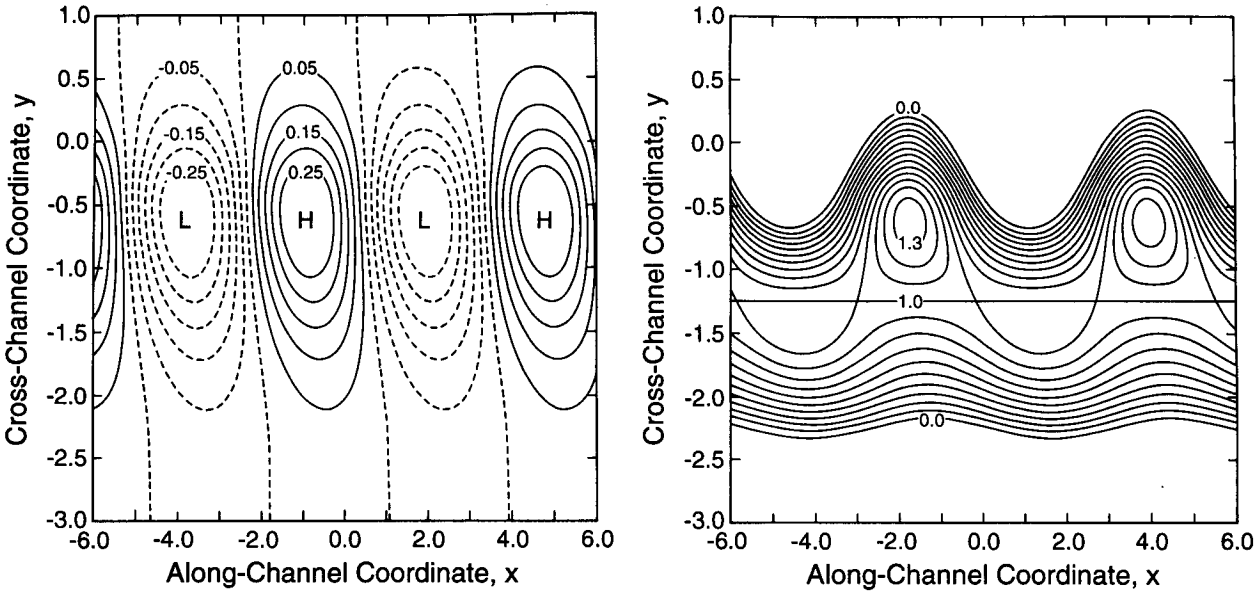

FIG. 7. Horizontal contour plots for the most unstable mode for $\mu = 1$. (a) The perturbation pressure. (The contour interval is 0.05.) (b) The total frontal height. (The contour interval is 0.1.) The instability appears as a series of growing, propagating anticyclones on the downslope side of the gravity current.

associated with deep-water replacement (LeBlond et al. 1991) in the Strait of Georgia. Our model is based on the nonquasigeostrophic theory developed by Swaters (1991) for the convective instability of a density-driven current on a sloping bottom. This is a model that explicitly filters out horizontal shear-based instabilities and the destabilization associated with a coupling of two lateral free streamlines.

Our calculations indicate that the deep-water replacement current is unstable. For parameter values reflective of the data as seen at cyclesonde station 3 in Stacey et al. (1987) or LeBlond et al. (1991), our calculations suggest a most unstable mode with a wavelength of about 40 km and an e-folding growth timescale of about one day. The wavelength is somewhat larger than the length scales suggested by the objective analysis of Stacey et al. (1988). However, the wavelength of the most unstable mode is rather sensitive to the choice of parameter values, and it can be argued that for environmental parameter values located near but not exactly at cyclesonde station 3 in Stacey et al. (1987) the wavelength of the most unstable mode is reduced by a factor of almost 2. The rapid timescale of the instability is encouraging since it suggests there is sufficient time for the finite-amplitude development of these unstable modes into small-scale eddylike anomalies with a characteristic radius of approximately 10 km. This is an estimate that is close to the objective analysis results of Stacey et al. (1988) for the subsurface anomalies.

The origin and structure of the low-frequency current fluctuations in the SOG are not completely understood. In particular, the spatial and temporal variability of the fluctuations has not been adequately resolved. Many explanations have been proposed for these fluctuations ranging from bottom-trapped vorticity waves or Kelvin waves to classical baroclinic/barotropic instability. All of these explanations have been problematic to some degree.

It may be that there is no single dominant source for these low-frequency fluctuations. However, we suggest that the rapid destabilization of the current associated with the deep-water replacement does address several aspects of the observations particularly in regards to the observed horizontally localized and seasonally variable nature of the conditions for baroclinic instability and the fact that the instability seems to occur at depth.

Whether or not, in fact, the convective instability of the water mass associated with the deep-water replacement in the SOG is the primary source of these fluctuations cannot be definitely resolved with the available datasets. Clearly, an observational program designed to monitor the evolution in time and space of the this water mass would go a long way to answer this question.

Acknowledgments. Preparation of this manuscript was supported in part by a research grant awarded by the Natural Sciences and Engineering Research Council of Canada (NSERC) and a science subvention awarded by the Department of Fisheries and Oceans of Canada to G. E. S. and a NSERC Postgraduate Scholarship awarded to R. H. K. We also thank the referees for their comments, which led to a substantially improved paper.

REFERENCES

Abramowitz, M., and J. A. Stegun, 1972: *Handbook of Mathematical Functions.* Dover Press, 1046 pp.

Chang, P., S. Pond, and S. Tabata, 1976: Subsurface currents in the Strait of Georgia, west of Sturgeon Bank. *J. Fish. Res. Board Can.,* **33,** 2218–2241.

Griffiths, R. W., P. D. Killworth, and M. E. Stern, 1982: Ageostrophic instability of ocean currents. *J. Fluid Mech.,* **117,** 343–377.

Helbig, J. A., and L. A. Mysak, 1976: Strait of Georgia oscillations: Low frequency currents and topographic planetary waves. *J. Fish. Res. Board Can.,* **33,** 2329–2339.

LeBlond, P. H., 1983: The Strait of Georgia: Functional anatomy of a coastal sea. *Can. J. Fish Aquat. Sci.,* **40,** 1033–1063.

——, and L. A. Mysak, 1978: *Waves in the Ocean.* Elsevier, 602 pp.

——, H. Ma, F. Doherty, and S. Pond, 1991: Deep and intermediate water replacement in the Strait of Georgia. *Atmos.-Ocean,* **29,** 288–312.

Nof, D., 1983: The translation of isolated cold eddies on a sloping bottom. *Deep-Sea Res.,* **30**(2A), 171–182.

Paldor, N., and P. D. Killworth, 1987: Instabilities of a two-layer coupled front. *Deep-Sea Res.,* **34,** 1525–1539.

Stacey, M. W., S. Pond, P. H. LeBlond, H. J. Freeland, and D. M. Farmer, 1987: An analysis of the low-frequency current fluctuations in the Strait of Georgia, from June 1984 until January 1985. *J. Phys. Oceanogr.,* **17,** 326–342.

——, ——, and ——, 1988: An objective analysis of the low-frequency currents in the Strait of Georgia. *Atmos.-Ocean,* **26,** 1–15.

——, ——, and ——, 1991: Flow dynamics in the Strait of Georgia, British Columbia. *Atmos.-Ocean,* **29,** 1–13.

Swaters, G. E., 1991: On the baroclinic instability of cold-core coupled density fronts on a sloping continental shelf. *J. Fluid Mech.,* **224,** 361–382.

Yao, T., S. Pond, and L. A. Mysak, 1982: Low frequency subsurface current and density fluctuations in the Strait of Georgia. *Atmos.-Ocean,* **20,** 340–356.

——, ——, and ——, 1985: Profiles of low frequency subsurface current fluctuations in the Strait of Georgia during 1981 and 1982. *J. Geophys. Res.,* **90,** 7189–7198.